Insights into the oxidation of organic contaminants by iron nanoparticles encapsulated within boron and nitrogen co-doped carbon nanoshell: Catalyzed Fenton-like reaction at natural pH

Hao Zhou[a,b,c], Shikang Wu[a], Yaoyu Zhou[a,f,*], Yuan Yang[a], Jiachao Zhang[a], Lin Luo[a], Xiaoguang Duan[d], Shaobin Wang[d], Lei Wang[e,f], Daniel C.W. Tsang[f,**]

[a] College of Resources and Environment, Hunan Agricultural University, Changsha 410128, China
[b] State Key Laboratory of Organic Geochemistry, Guangzhou Institute of Geochemistry, Chinese Academy of Sciences, Guangzhou 510640, China
[c] University of Chinese Academy of Sciences, Beijing 100049, China
[d] School of Chemical Engineering, The University of Adelaide, Adelaide, SA 5005, Australia
[e] Department of Materials Science and Engineering, The University of Sheffield, Sir Robert Hadfield Building, Mappin St, Sheffield S1 3JD, United Kingdom
[f] Department of Civil and Environmental Engineering, The Hong Kong Polytechnic University, Hung Hom, Kowloon, Hong Kong, China

ARTICLE INFO

ABSTRACT

Iron nanoparticles encapsulated within boron and nitrogen co-doped carbon nanoshell (B/N-C@Fe) were synthesized through a novel and green pyrolysis process using melamine, boric acid, and ferric nitrate as the precursors. The surface morphology, structure, and composition of the B/N-C@Fe materials were thoroughly investigated. The materials were employed as novel catalysts for the activation of potassium monopersulfate triple salt (PMS) for the degradation of levofloxacin (LFX). Linear sweep voltammograms and quenching experiments were used to identify the mechanisms of PMS activation and LFX oxidation by B/N-C@Fe, where $SO_4 \cdot^-$ as well as $HO\cdot$ were proved to be the main radicals for the reaction processes. This study also discussed how the fluvic acid and inorganic anions in the aqueous solutions affected the degradation of LFX and use this method to simulate the degradation in the real wastewater. The synthesized materials showed a high efficiency (85.5% of LFX was degraded), outstanding stability, and excellent reusability (77.7% of LFX was degraded in the 5th run) in the Fenton-like reaction of LFX. In view of these advantages, B/N-C@Fe have great potentials as novel strategic materials for environmental catalysis.

1. Introduction

In recent years, the fate and impacts of pharmaceuticals and personal care products (PPCPs) have received increasing attention worldwide which include numerous chemical classes and could pose potential risk to ecological and human health (Wang et al., 2010b). Pharmaceuticals are commonly used to treat or prevent human and animal bacterial infections along with promoting the growth in agriculture, aquaculture, and husbandry (Zhou et al., 2018a). Antibiotics belong to the class of pharmaceuticals whose consumption has increased considerably over the years (Zhou et al., 2017). With the increasing abuse of these chemicals, a large volume of antibiotics are entering the environment via discharge of sewage effluents due to incomplete elimination during conventional wastewater treatment processes, illegal discharge of untreated wastewater from factories, or direct excretion and emission in husbandry and aquaculture (Tran et al., 2018; Zhou et al., 2018a), resulting in water pollution and potential threat to human and aquatic life (Wang et al., 2019). Furthermore, antibiotics could re-enter the water and human body through the food chain.

The levofloxacin (LFX), a new kind of fluoroquinolones (FQs) which is usually resistant to traditional wastewater treatment including biological and chemical processes (Liu et al., 2017; Yan et al., 2017), is a synthetic broad-spectrum antibiotic used to treat severe or life-threatening bacterial infections such as tuberculosis, acute bacterial sinusitis, pneumonia, and even human-immunodeficiency-virus (HIV) infection (Goodwin et al., 1994; Hamdi El Najjar et al., 2013; Van Doorslaer et al., 2014; Xu et al., 2017). Therefore, LFX can be chosen as the target PPCPs to determine the degradation effect using our catalytic system. The total amount of LFX used in 2011 in human medicine was over 55
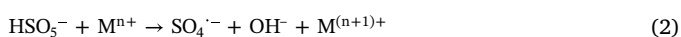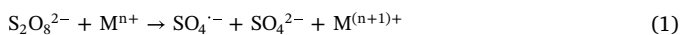
tons, which ranked second in the FQs consumption in the U.S. (Yan et al., 2017). In addition, it is reported that the total amount of FQs including 8 classes consumed in China was up to 27,300 tons (Zhang et al., 2015b). EPI Suite was used to determine the half-life of LFX in the air, water, soil, and sediment. Although the half-life of LFX in the air is 1.29 h, the half-lives in the water, soil, and sediment are 4320 h, 8640 h, and 38,900 h, respectively. As LFX cannot be quickly degraded in the natural environment, the water contaminated by LFX may possess a risk to human health and ecosystems.

Owing to the generation of highly reactive radicals such as $HO\cdot$, $O_2\cdot^-$, $\cdot OOH$ and $SO_4\cdot^-$ in advanced oxidation processes (AOPs), many organic contaminants can be effectively degraded into lower molecular compounds or even H_2O and CO_2 (Wang et al., 2016b; Yao et al., 2016). Among these highly reactive radicals, $SO_4\cdot^-$ plays a more promising performance in decomposing some refractory hazardous organic compounds compared with $HO\cdot$, owing to its ability of selective oxidation and wide pH adaptability (Anipsitakis and Dionysiou, 2003; Duan et al., 2015a; Zeng et al., 2015; Zhao et al., 2017). The redox potential for $HO\cdot$ and $SO_4\cdot^-$ are 1.9–2.7 V and 2.5–3.1 V, respectively (Zeng et al., 2015; Zhou et al., 2018b), whereas $SO_4\cdot^-$ can be activated by ultraviolet light, heat, and transition metals. Among these methods, transition metals (e.g., Fe^{2+}, Co^{2+}, and Mn^{2+}) mediated activation of potassium monopersulfate triple salt (PMS, $2KHSO_5\cdot KHSO_4\cdot K_2SO_4$) has received considerable attention as this process can work in mild conditions, produce almost no byproduct sludge after reaction (Lei et al., 2015; Wei et al., 2015). Also, the natural reserve of transition metals, especially iron, is abundant. The mechanisms of transition metal mediated activation of persulfate including PMS can be described by Eqs. (1) and (2).

$$S_2O_8^{2-} + M^{n+} \rightarrow SO_4^{\cdot-} + SO_4^{2-} + M^{(n+1)+} \tag{1}$$

$$HSO_5^- + M^{n+} \rightarrow SO_4^{\cdot-} + OH^- + M^{(n+1)+} \tag{2}$$

Iron-based nanoparticles (Fe-NPs) as heterogeneous catalysts have been particularly studied because Fe-NPs can perform an excellent degradation efficiency and iron is highly accessible because iron is the second most abundant metallic element in the earth's crust (Du and Eisenberg, 2012; Sun et al., 2017). In addition, Fe-NPs can be easily separated from the aqueous solutions using an external magnetic field (Zhou et al., 2014; Lei et al., 2018), which is easy for the reuse of Fe-NPs materials. However, conventional Fe-NPs are unstable and are easily deactivated due to aggregation and leaching during the reaction progress. In addition, the general preparation methods require sonication. Some of them also use argon gas, even hydrogen sulfide gas, etc., which increases the fabrication cost and the risk of handling (Huang et al., 2018b; Wang et al., 2018). Novel Fe-NPs need to be developed to solve this problem and core-shell materials are regarded as an excellent solution. Metal-based catalysts encapsulated by a protective shell have been proven to enhance the catalytic performance and stability (Wang et al., 2017). The protective organic or inorganic shells are usually prepared at lower temperatures, which limits the application of potential Fe-NPs catalysts (Cui et al., 2015; Ghosh Chaudhuri and Paria, 2012; Sun et al., 2018). Thus, more efficient and stable Fe-NPs should be developed, and doping of foreign atoms is one of the most effective approaches.

The doping of iron-based catalysts with heteroatoms offers a practical path to adjust the properties of the catalysts by creating new states that modify their electronic structure and to improve the catalytic performance by enhancing the reactivity and electrical conductivity (Ali et al., 2017; Sun et al., 2019; Yu et al., 2019). Iron nanoparticles encapsulated within boron and nitrogen co-doped carbon nanoshell was put forward because boron as electron acceptor and nitrogen as electron donor are one electron away from carbon. N-doped carbon nanotubes have recently gained a noticeable popularity as low-cost catalysts, owing to the high abundance of catalytic sites, environmental compatibility, and long-term operation stability (Chen et al., 2014; Gong

et al., 2009). N-doped materials are demonstrated to produce defects in catalysts, which results in the formation of the O_2 absorption active sites and increases the activity in oxidative dehydrogenation (Cui et al., 2015; Xiong et al., 2017). Similarly, B-doped carbon materials can break the electroneutrality of carbon-based materials, change the electronic structure, and enhance the electrical properties of carbon-based materials by creating active sites (Wang et al., 2014a). Meanwhile, the introduction of boron also increases the number of hole-type charge carriers, which enhance the conductivity of the material (Kim et al., 2012). Although many studies have proposed the preparation methods of B-doped nanomaterials and N-doped nanomaterials and applied them to oxygen reduction catalysts, lithium-ion batteries, and sodium-ion batteries (Li et al., 2018; Wang et al., 2014a; Wang et al., 2018; Zhang et al., 2015a), B, N co-doped nanomaterials have not been widely used in PPCPs contaminated wastewater treatment. The most common doping method is by direct pyrolysis, which allows for control over the porosity and structure by choosing the right substrate and reagents (Ratso et al., 2018). In addition, use of waste or renewable material, less hazardous process, and less carbon footprint associated with the resource mining are the advantages of this method of synthesis.

Herein, we developed a novel and simple strategy for the controlled synthesis of iron nanoparticles encapsulated within boron and nitrogen co-doped carbon nanoshell (B/N-C@Fe) through the direct pyrolysis of melamine, boric acid, and ferric nitrate. The properties of B/N-C@Fe to activate PMS in degradation of LFX and the mechanisms of degradation were evaluated and elucidated in detail. Various characterization techniques were applied to investigate and characterize the morphologies, compositions, and active sites of synthetic materials.

2. Materials and methods

2.1. Materials and chemicals

Melamine ($C_3H_6N_6 > 99.0\%$) and ferric nitrate nonahydrate (Fe $(NO_3)_3\cdot 9H_2O > 98.5\%$), purchased from Sinopharm Chemical Reagent Co., Ltd., and boric acid ($H_3BO_3 > 99.5\%$), purchased from Shanghai Macklin Biochemical Co., Ltd. were the precursor chemicals to synthesize B/N-C@Fe. Levofloxacin ($C_{18}H_{20}FN_3O_4 > 98.0\%$) were purchased from Shanghai Huzhen Biological Technology Co., Ltd. Potassium monopersulfate triple salt (PMS, $2KHSO_5\cdot KHSO_4\cdot K_2SO_4 > 47\%$ $KHSO_5$ basis) were purchased from Aladdin Industrial Corporation. Fluvic acid ($C_{14}H_{12}O_8$, 85%) and p-Benzoquinone ($C_6H_4O_2$, 97%) were purchased from Shanghai Macklin Biochemical Co., Ltd. The remaining chemicals, including tricobalt tetraoxide (Co_3O_4), ferrous sulfate heptahydrate ($FeSO_4\cdot 7H_2O$), sodium bicarbonate ($NaHCO_3$), sodium formate ($HCOONa$), sodium chloride ($NaCl$), disodium hydrogen phosphate dodecahydrate ($Na_2HPO_4\cdot 12H_2O$), sodium dihydrogen phosphate dihydrate ($NaH_2PO_4\cdot 2H_2O$), sodium sulfate (Na_2SO_4), sodium acetate anhydrous (CH_3COONa), sodium nitrate ($NaNO_3$), tert-Butanol ($C_4H_{10}O$), methanol anhydrous (CH_3OH), hydrochloride acid (HCl), and acetone (CH_3COCH_3), were purchased from Sinopharm Chemical Reagent Co., Ltd. All chemicals were of analytical grade and used without further purification. Ultrapure water produced by a Milli-Q water purification system (18.25 MΩ cm) at room temperature was used in all of the experiments.

2.2. Synthesis of B/N-C@Fe

B/N-C@Fe catalysts were fabricated via a facile thermal process using $C_3H_6N_6$ as a C/N precursor, H_3BO_3 as a B precursor, and Fe $(NO_3)_3\cdot 9H_2O$ as a Fe precursor. In a typical procedure, 0.06 mol $C_3H_6N_6$, 0.12 mol H_3BO_3, and a designed loading (3, 4, 6, 12 mmol) of Fe(NO_3)$_3\cdot 9H_2O$ were dissolved in 400 mL of ultrapure water at 85 °C with continuous stirring for 3 h to form a brown-yellow muddy mixture. Subsequently, the resulting mixture was placed in an oven at 110 °C in the air overnight. After drying, the resulting materials were ground into

powders < 0.25 mm in an agate mortar. The dried powders were transferred into a quartz tube furnace to anneal at 600 °C, 700 °C, 800 °C, and 900 °C, respectively, with a heating rate of 5 °C min^{-1} and held at the designated temperature for 3 h under a nitrogen flow of 50 mL min^{-1}. After cooling down to room temperature under ambient atmosphere, the as-obtained dark grey materials were treated with 100 mL hydrochloric acid (36 to 38, wt%) with magnetic stirring for 6 h to remove any weakly bound, acid-accessible iron species. The materials were then washed with ultrapure water and acetone 3 times, respectively. In the end, the materials were dried at 60 °C for 6 h and ground into powders < 0.25 mm for future use. The obtained catalysts were magnetic powders and named as B/N-C@FeX T (where T represents the calcination temperature of the materials and X represents the molar amount of Fe(NO$_3$)$_3$·9H$_2$O added).

2.3. Characterization of catalysts

X-ray diffraction (XRD) patterns were acquired on a Bruker D8 Advance X-ray instrument using Cu-Kα radiation with λ at 1.5418 Å operating at 40 kV/40 mA and the data were acquired with a fixed divergence slit of 0.02° in the range of 10–80° (2θ) at the scan speed of 6° min^{-1}. Thermogravimetric analysis (TGA) was performed using a TA Instrument SDT Q600 within a temperature range of 50-900 °C at a heating rate of 10 °C min^{-1} under nitrogen atmosphere. Field-emission scanning electron microscopy (FE-SEM, SU8010, Hitachi) and field-emission transmission electron microscopy (FE-TEM, JEM-2100F, JEOL) were applied to investigate the morphologies of the catalysts. Energy dispersive X-ray spectrometer (EDS, GENESIS, EDAX) analyses were performed during the high-resolution transmission electron microscopy (HRTEM). The chemical compositions and states of the catalysts were determined by X-ray photoelectron spectroscopy (XPS), which was carried out on a Thermo Escalab 250 Xi instrument with Al-Kα X-rays. Electrochemical characterization was carried out with CHI760E electrochemical workstation (CH Instrument, Chenhua, Shanghai, China) in a three-electrode cell system at ambient atmosphere, using a Pt wire as the counter electrode and the B/N-C@Fe catalyst on a glassy carbon electrode as the working electrode. The reference electrode of linear sweep voltammetry (LSV) polarization is Ag/AgCl electrode.

2.4. Catalytic oxidation of LFX

The catalytic oxidation was carried out in a 100 mL vial with LFX solution (50 mg L^{-1}, 50 mL), the PMS (2.0 g L^{-1}) and the B/N-C@Fe catalyst (0.2 g L^{-1}) at constant temperature (25 ± 1 °C) controlled water bath under continuous stirring for the kinetic studies. The samples were taken out with a syringe at regular intervals, filtered with a 0.45 μm Millipore film. The tests have compared the degradation efficiency of various B/N-C@FeX T materials and then chose the best catalytic material. Some other catalysts, such as Fe(NO$_3$)$_3$·9H$_2$O, FeSO$_4$·7H$_2$O, and Co$_3$O$_4$, were used to compare the degradation effects on this aqueous system with the best synthetic material. The effects of reaction parameters (including PMS dosage, reaction temperature, fluvic acid, and various inorganic anions) were investigated as well. For selective experiments, tert-butanol (TBA), methanol anhydrous (MeOH), and p-benzoquinone (BQ) were used as probe compounds or scavengers to distinguish the HO· and SO$_4$·$^-$ radicals. To prove the recycling performance of the material, the used B/N-C@Fe catalysts were magnetically separated and then treated by ultrasonic washing with ultrapure water for 5 min and without any further treatment. The treated B/N-C@Fe catalysts were used in the next run at the same conditions. The recycling experiments were repeated for another four times. All the experiments were conducted at natural pH.

2.5. Analytical methods

The concentrations of leaching iron ions in the aqueous solutions were detected by atomic absorption spectroscopy (GF/FF-AAS, AA-6880, Shimadzu). The analysis of total organic carbon (TOC) was performed with a TOC analyzer (Elementar Vario TOC Cube, Elementar). The time-concentration of LFX was analyzed by high performance liquid chromatography (HPLC, Agilent 1100, Agilent). Column: Agilent HC-C18, 5 μm, 4.6 mm × 250 mm, at room temperature. The mobile phase was composed of 0.01 M oxalic acid/methanol/acetonitrile (45:20:35, V/V) mixture at 1 mL min^{-1}, and the UV detector was selected at λ = 293 nm.

3. Results and discussion

3.1. Properties of B/N-C@Fe catalysts

Various B/N-C@Fe materials were prepared by adjusting the molar amount of Fe(NO$_3$)$_3$·9H$_2$O and pyrolysis temperatures. Through the degradation experiments of LFX with various materials (shown in Fig. 3), B/N-C@Fe4 700 was found to be in the best efficiency in the preliminary experiment. Thus, various characterization techniques, including XRD, TGA, SEM, TEM, EDS, XPS and LSV, were used to characterize the properties of B/N-C@Fe4 700.

The XRD patterns of B/N-C@Fe3 700, B/N-C@Fe4 700, B/N-C@Fe6 700, B/N-C@Fe12 700, B/N-C@Fe4 600, B/N-C@Fe4 800 and B/N-C@Fe4 900 are presented to describe the crystallographic structures in Fig. 1. The sharp diffraction peak at 2θ of 26.4° is indexed to (002) planes of the graphitic carbon (JCPDS 35-0772) and the intensity increased with the increasing molar amount of Fe(NO$_3$)$_3$·9H$_2$O and pyrolysis temperatures, compared to the graphitic carbon and carbon nanoshell. The broad reflections centered at ca. 26° can be attributed to the presence of intercalated N-defects in the nitrogen-doped carbon structure (Wang et al., 2016a). The samples had a strong and sharp peak at a 2θ of 44.6°, which is assigned to (110) planes of α-Fe (JCPDS 06-0696) and demonstrates that the materials contain traces of metallic iron as Fe$_3$C (Wang et al., 2017; Sun et al., 2019). This suggests that Fe^{3+} was partly reduced to Fe^0 by as-formed carbon during the heating process in the N$_2$ atmosphere (Yao et al., 2016). It can be concluded from the XRD patterns that the iron nanoparticles were encapsulated in carbon nanotubes which could be well preserved during the reaction, as the leaching process showed that the concentration of iron ion in the aqueous solutions is 0.47 mg L^{-1}. Moreover, we can see from Fig. S1 that both of the two main sharp peaks at 26.4° and 44.6° were also found in the XRD patterns after the catalytic reaction. This suggests that the material is stable enough to be reused, which can be confirmed by the recycling experiment below.

The TGA plots (Fig. S2) of B/N-C@Fe materials all showed a decreased weight tendency from room temperature to ca. 800 °C and the majority of them showed a slight weight increase above 800 °C. The weight loss below 200 °C can be assigned to the evaporation of adsorbed water molecules on the surface of the materials, whereas the weight loss between 600 °C and 800 °C is associated with the release of the structure water (Wang et al., 2010a). The weight loss between 250 °C and 450 °C apart from two water loss events can be attributed to the destruction of amorphous carbon and deoxygenation of labile oxygenated functional groups on the surface of the materials, such as −OH and C=O in the forms of H$_2$O, CO, and CO$_2$ (Wang et al., 2014b; Yu et al., 2019). Also, the transformation of Fe$_3$C into Fe$_2$O$_3$ in the range of 360 °C to 550 °C can result in a weight loss (Wang et al., 2017; Sun et al., 2019). A slight weight increase can be observed over 800 °C, resulting from the oxidation of iron in the air atmosphere (Shen et al., 2015). Through the TGA plots, we can observe that the molar amount of iron as well as the pyrolysis temperature have a significant influence on the morphology and graphitization of carbon. In addition, the curve of
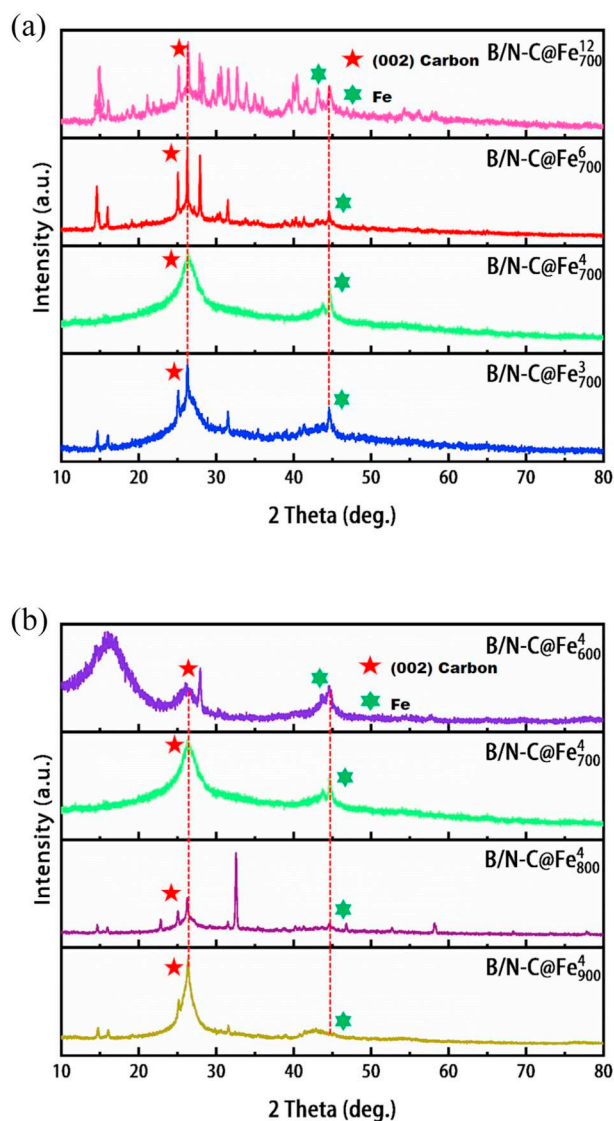
Fig. 1. XRD patterns of various B/N-C@Fe catalysts prepared at different (a) Fe(NO$_3$)$_3$·9H$_2$O dosages and (b) pyrolysis temperature.

the most effective catalyst was similar to our previous findings (Yao et al., 2016).

As revealed in the FE-SEM and FE-TEM images (Fig. 2a, b), the material consists of randomly oriented and entangled carbon nanoshells, and the pea-pod dark iron carbide nanocrystals were encapsulated in the well-defined carbon nanoshells, suggesting an efficient assembly between the Fe-NPs and the carbon nanoshell. From the enlarged TEM image (Fig. 2b), the outer diameter of the nanotube is in a range of 25–95 nm, with the wall thickness in a range of 3–15 nm. The iron nanoparticles are coated with graphitic carbon by 8–12 layers. EDS analysis (Fig. S3) shows the major element components in the synthetic material, such as C, Fe, Cu. Such a geometric confinement of iron carbide with maghemite and other iron hydroxides within carbon nanoshells can enhance their interfacial contact and suppress the dissolution and agglomeration of core materials, thereby promoting the electrochemical activity and stability of the hybrids (Wu et al., 2012).

3.2. Removal of LFX by PMS in combination with B/N-C@Fe

The results (Fig. 3) showed that the structure differences between materials have a significant impact on activating PMS in the degradation of LFX as analyzed by XRD and TGA. Owing to the specific structure, B/N-C@Fe4 700 exhibits a better performance with almost 80% of LFX being degraded in the first 5 min. This inferred that the B/N-C@Fe4 700 catalyst, with wide carbon nanoshells open at both ends, was more accessible to promote the catalytic reactions because of the full contact of LFX molecular and Fe$_3$C in a relatively restricted area (Shi et al., 2016). We have performed the adsorption experiments (Fig. S5) and the removal of LFX was not significant. Only 9.4% of LFX was removed after 120-min adsorption. At the beginning of the degradation experiments, under the action of adsorption and advanced oxidation, LFX was rapidly degraded. As time progressed, PMS was further degraded to some extent during advanced oxidation. Our recent study has revealed that PMS showed continuous decomposition with reaction time and the amount of PMS decreased by about 40% in the first 10 min (Kang et al., 2018).

Some frequently used catalysts, such as Fe(NO$_3$)$_3$·9H$_2$O, FeSO$_4$·7H$_2$O, and Co$_3$O$_4$, were employed to compare the efficiency of synthetic material and other Fenton-like catalysts. It can be found that all of these catalysts showed much weaker abilities in activating PMS for the LFX degradation (Fig. 4). However, Fe(NO$_3$)$_3$·9H$_2$O and FeSO$_4$·7H$_2$O were able to activate PMS, leading to 26.5% and 36.1% LFX oxidation after 20 min of reaction, respectively. This phenomenon indirectly indicated that the redox of Fe^{2+} and Fe^{3+} has a significant influence on the activation of PMS. The results showed that B/N-C@Fe4 700 is the most active catalyst under our experimental conditions.

X-ray photoelectron spectra (XPS) studies were carried out to further investigate the chemical composition and electronic structure of the B/N-C@Fe4 700 catalyst before and after the degradation experiment. Fig. S4 shows the XPS spectra, in which the five elements including Fe, O, C, B, and N existed in both catalysts before and after the reaction. Although Fe was detected by XRD, SEM, and TEM, the XPS spectra revealed relatively low surface contents of Fe on both catalysts, implying the significance of catalytic reaction and subsequent leaching of surface iron species within 5–10 nm probing depth of XPS analysis. This result corresponded to the detected Fe leaching (0.47 mg L^{-1}). This further proved that the Fe$_3$C nanoparticles were entirely encapsulated by carbon layers in the catalysts, which can thus survive the catalytic process (Wang et al., 2017).

The high resolution curve-fitted elementary XPS peaks of N 1s, B 1s, C 1s, and O 1s are displayed in Fig. 5a–d. The N 1s spectra were deconvoluted into two peaks at 398.3, 399.1, and 400.0 eV, assigned to pyridinic N, N—C bonds, and graphitic N, respectively. The peak at a binding energy of 398.3 eV also includes a contribution from nitrogen bound to the Fe metal (Fe—N), due to the marginal difference between binding energies of Fe—N and pyridinic N (Liang et al., 2013). Pyridinic N is regarded as the major contributor of the catalytic activity because of its reduction of the energy barrier for adsorbing reactants on adjacent carbon atoms and its acceleration of rate-limited first-electron transfer (Soares et al., 2015). Because of the coverage of graphitic N layers on the Fe$_3$C surface, no obvious Fe signal can be detected (Xiao et al., 2015). The peak at 399.1 eV is mainly caused by melamine containing C=N—C structure (Soares et al., 2015). Pyridinic N and graphitic N are believed to play an important role in activating N species toward oxygen reduction reaction (Peng et al., 2014).

The XPS spectra of B 1s were fitted into two components, assigned to h-BN at 190.7 eV and C-NB group at 192.2 eV, which indicates that boron atoms have been introduced into carbon frame (Yan et al., 2010). This structure is attributed to the bond of BC$_2$O and BCO$_2$ (Zhang et al., 2015a). The analysis of C 1s level (Fig. 5c) identified four components that were assigned to C—C at 284.8 eV, hydroxyl C—OH at 285.7 eV, C—N at 287.2 eV, and carbonyl C=O at 288.4 eV, respectively (Xiao et al., 2015; Yao et al., 2016). The O 1s spectra can be divided into four components related to the presence of O—Fe bonds (530.3 eV), defective oxides and hydroxides (531.5 eV), O—B bonds (532.5 eV), and O—N bonds (533.7 eV), respectively (Yao et al., 2016). It can be seen from Fig. 5d that the peaks at 531.5 eV and 532.5 eV have increased while the peak at 533.7 has decreased, due to the reduction of iron oxides
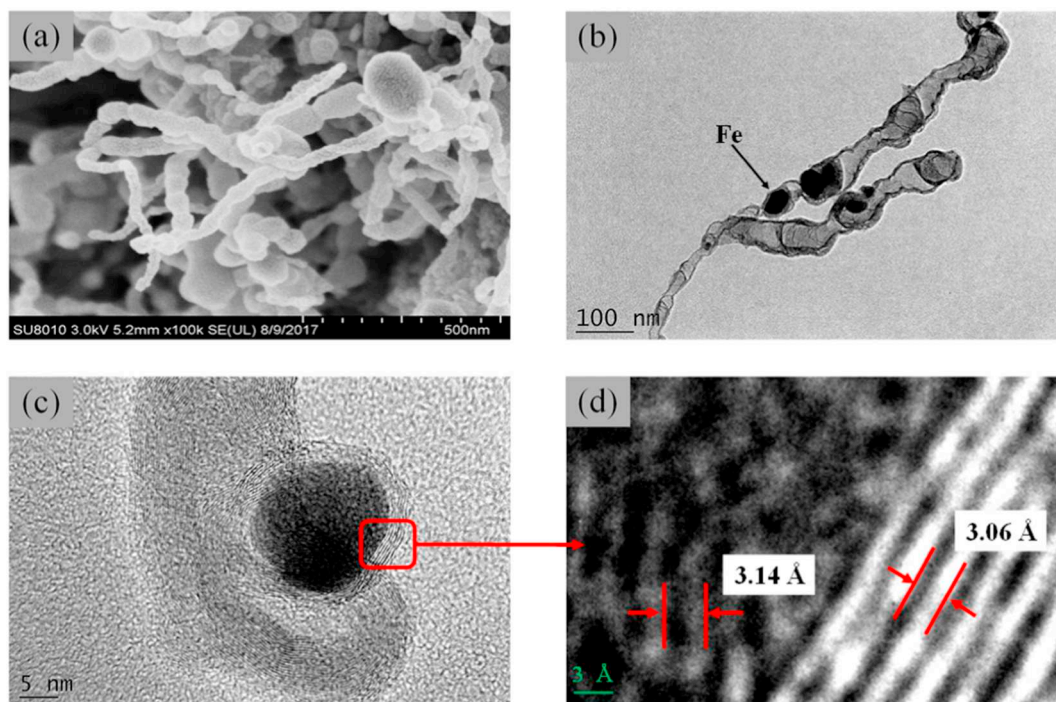
Fig. 2. (a) FE-SEM, (b) FE-TEM and (c, d) HRTEM images of B/N-C@Fe$_{700}$[4] catalyst.

(Zhang et al., 2014). Because of the redox reaction during the Fenton-like process, a slightly positive shift of binding energies was observed after the LFX degradation.

3.3. Effects of operating conditions and solution chemistry on LFX removal

As B/N-C@Fe4 700 displayed the best activity, the LFX degradation efficiency under the effects of varying PMS dosage, reaction temperature, and co-existing anions are discussed for the use of B/N-C@Fe4 700. As shown in Fig. 6a, the degradation efficiency increased along with the increasing PMS dosage up to $2\,g\,L^{-1}$, resulting in the formation of an elevated amount of radicals during the Fenton-like process. However, beyond $2\,g\,L^{-1}$ PMS dosage, the degradation efficiency has decreased slightly, possibly due to the self-scavenging and the increase in turbidity of solution during the reaction (Sharma et al., 2015). Hence, the optimized PMS concentration was $2\,g\,L^{-1}$.

Fig. 6b shows that with the increase of temperature from 25 to 60 °C, the degradation efficiency first decreased till 35 °C and then increased till 60 °C. When the temperature below 35 °C, the increased turbidity of the solution may limit the reaction process; and then with further increase in temperature, the activation by thermal energy can counteract this negative effect. In addition, the increase in temperature can result in the decomposition of PMS, which will enhance the generation of radicals (Yao et al., 2015b).

Fig. 6c shows that almost all of the studied inorganic anions have a negative impact on the LFX degradation. In this study, the negative effect of these inorganic anions was found to be in the following order: $HCOO^- > H_2PO_4^- > SO_4^{2-} > NO_3^- > CH_3COO^- > HPO_4^{2-} > HCO_3^- > Cl^-$. The negative effect of inorganic anions is attributed to the competitive adsorption between anions and the target organic compounds onto the surface of the catalyst. It is believed that the competitive adsorption or blockage of the active sites may hinder the catalytic degradation of organic substance by oxidative species (Eskandarloo et al., 2014). It can be vividly seen from Fig. 6c that when chloride ions are present, the initial degradation rate is slightly improved. The HO· generated by the reaction reacts with Cl^- to form

$ClOH·^-$, and further generated Cl· under the action of H^+, thereby accelerating the degradation reaction (Huang et al., 2018a). The mechanism can be illustrated by Eqs. (3) and (4). In addition, $SO_4·^-$ can react with Cl^- to produce Cl·, which can accelerating the degradation reaction as well (Zhang et al., 2018). HO·, $SO_4·^-$, and Cl· (E^0(Cl·/Cl^-) = 2.4 V) are all strong oxidants (Zhang et al., 2018). In the presence of Cl^-, $SO_4·^-$ and HO· can be transformed into Cl· to some degree. There is little difference in their redox potential, while Cl· is a more selective oxidant than HO· (Miklos et al., 2018). Even though HO· has a slightly higher redox potential than Cl·, part of HO· may react with the transformation products rather than LFX itself. In addition, part of HO· is consumed by the reaction with Cl^- to form Cl·. We have also observed non-radical pathways in the LFX degradation, of which the relative significance warrants further investigation in future studies. All these factors may contribute to the initial improvement of LFX removal. Carboxylic acid and acetic acid chemicals can adjust pH conditions, form soluble surface complexes and complex with Fe, inducing the dissolution of metal oxides and hindering the generation of radicals (Tso and Shih, 2018). Ferrous carbonates precipitate would form on Fe surface in carbonate-bearing water, which may block the reactive and attachment sites on the Fe surface and reduce its reactivity (Tso and Shih, 2015). Fe^0 can serve as an electron donor to reduce nitrate (Su and Puls, 2004). Therefore, the presence of nitrate reduces the active site of Fe^0 and PMS reaction, thereby reducing the generation of free radicals.

$$HO· + Cl^- \rightarrow ClOH·^- \qquad (3)$$

$$ClOH·^- + H^+ \rightarrow Cl· + H_2O \qquad (4)$$
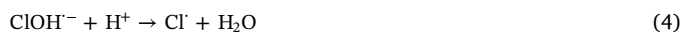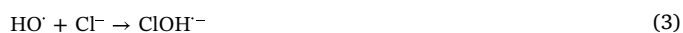
In order to better simulate the real degradation during the actual wastewater, fulvic acid (FA) was selected as the model natural organic matter (NOM). Because approximately 70% of NOM is composed of FA in nature (Yao et al., 2016). As can be seen in Fig. 7, only in the first 20 min, FA of all studied concentrations has a slightly negative effect on the LFX degradation. After 20 min, the degradation efficiency seems to be comparable with the reaction without FA, and the final degradation
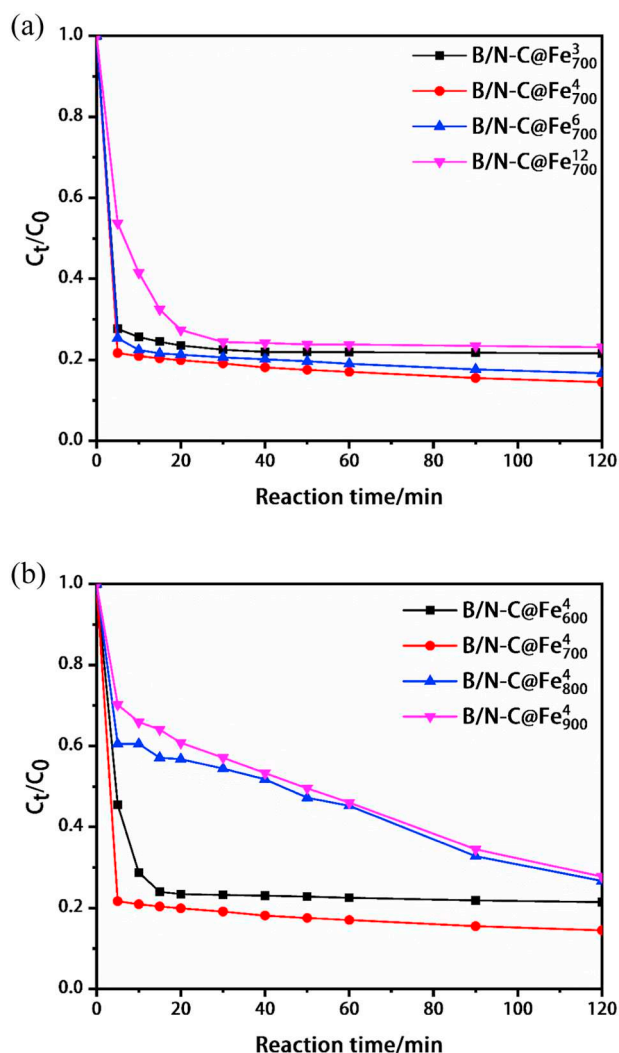
Fig. 3. Kinetic data of the degradation of LFX in the presence of PMS and B/N-C@Fe prepared at different (a) Fe(NO$_3$)$_3$·9H$_2$O dosages and (b) pyrolysis temperature. The reaction conditions are: [LFX] = 50 mg L^{-1}, [catalyst] = 0.2 g L^{-1}, T = 25 °C, [PMS] = 2 g L^{-1}, without pH adjustment.

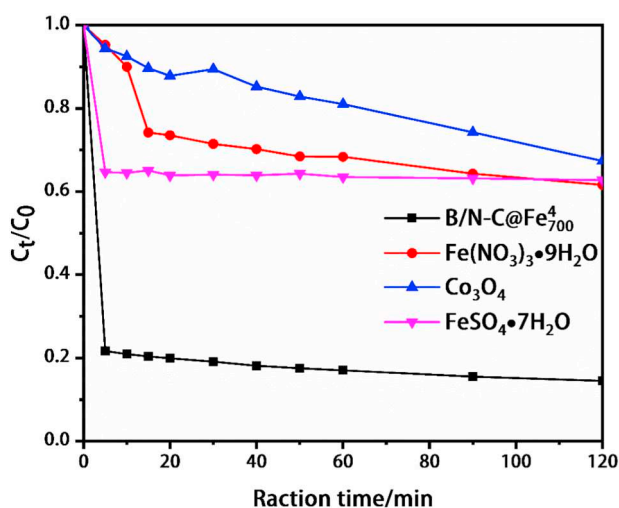**Fig. 4.** Comparison of the catalytic performance of different catalysts under the same condition. The reaction conditions are: [LFX] = 50 mg L^{-1}, [catalyst] = 0.2 g L^{-1}, T = 25 °C, [PMS] = 2 g L^{-1}, without pH adjustment.

efficiency exhibits only a little difference with or without FA. As a typical natural organic matter in water, FA was found to impose an inhibitory effect on the degradation of LFX under all the studied systems because FA can compete with LFX for HO· and SO$_4$·$^-$, the former in particular due to its low selectivity (Khan et al., 2013; Yao et al., 2015a). This result shows that our as-synthesized B/N-C@Fe4 700 catalyst has a great potential for practical engineering applications.

3.4. Reusability of B/N-C@Fe

The LFX removal was repeated for five cycles in the same catalytic system. As shown in Figs. 8, 77.7% of LFX could still be degraded after five cycling runs. This indicates that the as-synthesized nanomaterial B/N-C@Fe4 700 exhibits an excellent stability and reusability for the removal of organic pollutants. As shown in Fig. 8, the slight decline of degradation efficiency is likely due to the loss of active sites on the surface of B/N-C@Fe4 700 through the redox cycles and dissolution of reactive iron species on the surface (Figs. S1 and S4), oxidation of graphitic carbons (Fig. 5c, d), changes of pore structures (Fig. 2), and possible adsorption of LFX and its byproducts (Duan et al., 2015a; Lee et al., 2016). As mentioned above, the concentration of leaching iron was 0.47 mg L^{-1}, which is acceptable according to EU discharge standard (< 2 mg L^{-1}) (Deng et al., 2008).

In addition, as can be seen from Fig. S1, compared to fresh B/N-C@Fe4 700, the spinel crystalline form in the cubic phase appeared after the first run, suggesting that the catalyst is still stable. Nevertheless, the peak intensity of Fe$_3$C decreased after the first run, suggesting that some of the Fe$_3$C were consumed during the catalytic process. It is noteworthy that the reusability of B/N-C@Fe4 700 showed a better performance than those of N-doped graphene and N-doped carbon nanotubes (CNTs) (Duan et al., 2015b; Sun et al., 2014), implying that the inner stability of Fe$_3$C due to spinel crystalline formation after the first run may play an important role in the enhanced stability of our catalyst. Furthermore, the carbon nanoshell and iron carbide were in close proximity, which may result in the enhanced catalytic performance (Wang et al., 2015b). Even though the encapsulated Fe$_3$C nanoparticles are not in direct contact with the aqueous system, they still play a key role in the carbocatalysis with PMS activation. This role can be ascribed to the synergetic interaction between the iron carbide and protective graphitic layers (Hu et al., 2014). The inner Fe$_3$C can activate the peripheral graphitic carbon layers, rendering the outer surface of the graphitic carbon layer more reactive toward the aqueous system.

3.5. Mechanisms of PMS activation and LFX oxidation by B/N-C@Fe

From the above results, it is considered that the oxidizing species, which are the main approach for the degradation of organic contaminants, are produced from the B/N-C@Fe4 700/PMS system. In the presence of PMS, SO$_4$·$^-$ and HO· are considered to be the oxidizing species in the catalytic process (Zhou et al., 2015). Therefore, the removal of LFX by the B/N-C@Fe4 700/PMS system was examined in the presence of various oxidant scavengers at the same condition. MeOH is regarded as an effective quenching reagent for HO· ($k_{HO·}$ = 1.2–2.8 × 10^9 M^{-1} s^{-1}) and SO$_4$·$^-$ ($k_{SO4·_-}$ = 1.6–7.8 × 10^6 M^{-1} s^{-1}). For comparison, tert-butanol (TBA) is used as a quenching agent for HO· ($k_{HO·}$ = 3.8–7.6 × 10^8 M^{-1} s^{-1}) but not for SO$_4$·$^-$ ($k_{SO4._-}$ = 4–9.1 × 10^5 M^{-1} s^{-1}) (Guan et al., 2013; Zhang et al., 2013; Zou et al., 2013).

As shown in Fig. 9a, when TBA was added to the system, the degradation efficiency slightly decreased, indicating that a small amount of HO· was generated during the catalytic process. It seems that a relatively low concentration of MeOH has a slightly negative impact on the degradation (Fig. 9b). However, when the dosage of MeOH increased, there was a remarkable decrease of degradation efficiency and the inhibitory effect was greater than that of TBA. This indicates that the catalytic process generated SO$_4$·$^-$ radical as the main contributor to LFX degradation. When the concentration of MeOH increased to
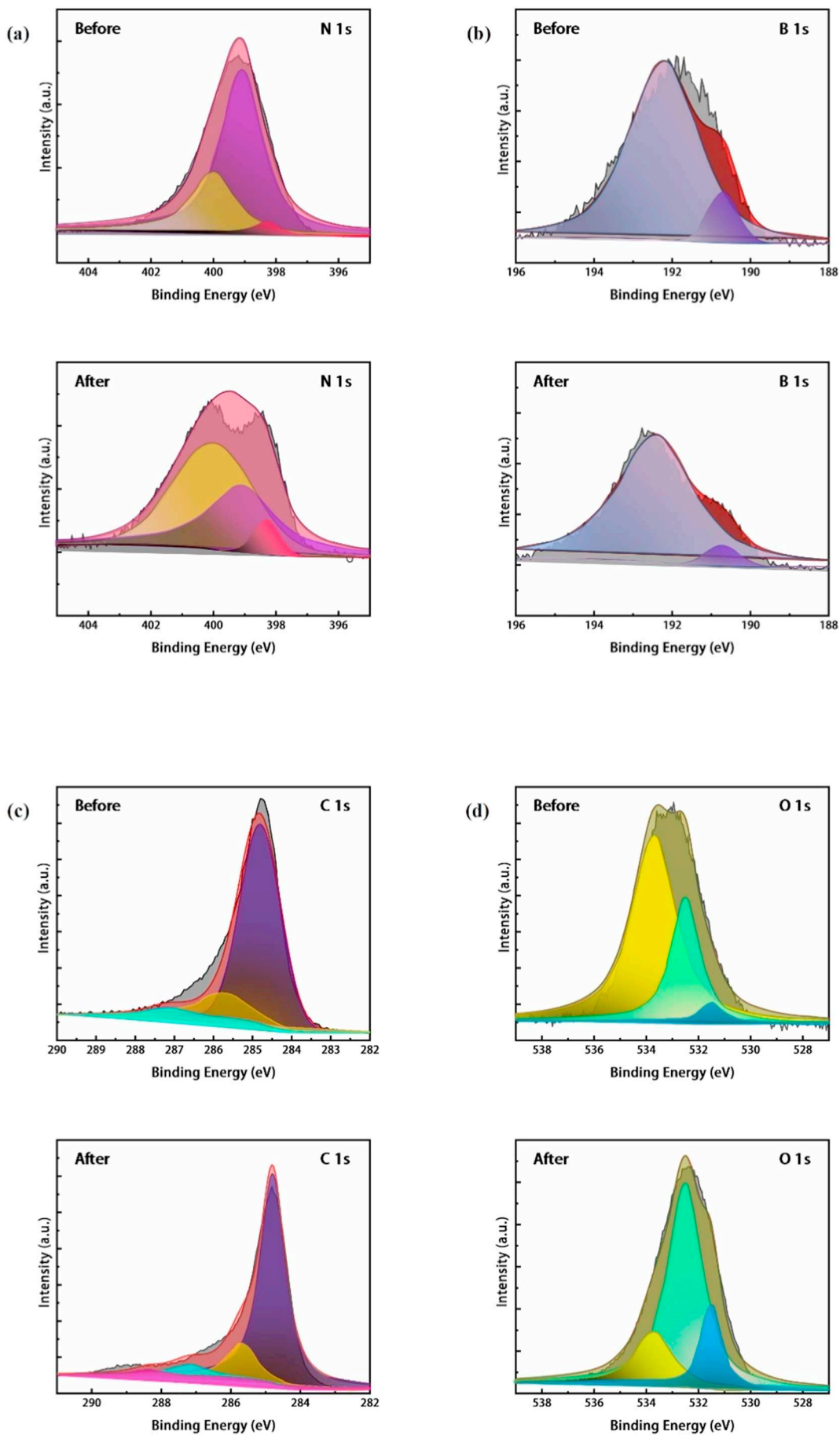
Fig. 5. (a) N 1s XPS spectra, (b) B 1s XPS spectra, (c) C 1s XPS spectra and (d) O1s XPS spectra of B/N-C@Fe$_{700}$[4] before and after the Fenton-like reaction.

Fig. 7. Effects of FA concentration on the degradation of LFX by the B/N-C@Fe$_{700}$^{4}/PMS process. The reaction conditions are: [LFX] = 50 mg L^{-1}, [catalyst] = 0.2 g L^{-1}, T = 25 °C, [PMS] = 2 g L^{-1}, without pH adjustment.

Fig. 8. Recycle experiments for LFX degradation using B/N-C@Fe$_{700}$^{4}. The reaction conditions are: [LFX] = 50 mg L^{-1}, [catalyst] = 0.2 g L^{-1}, T = 25 °C, [PMS] = 2 g L^{-1}, without pH adjustment.
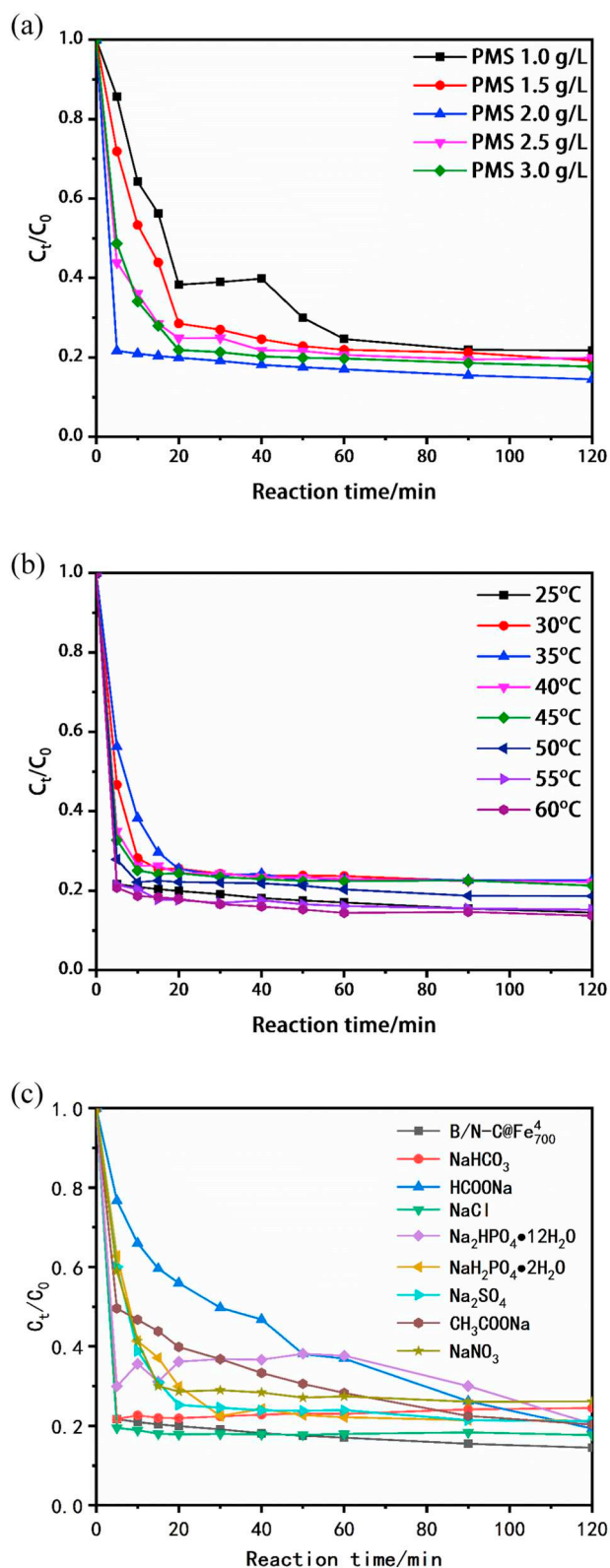

Fig. 6. Varying effects on the catalytic degradation of organic dyes: (a) different oxidizing dosage, (b) reaction temperature and (c) different anions. The reaction conditions are (unless otherwise stated): [LFX] = 50 mg L^{-1}, [catalyst] = 0.2 g L^{-1}, T = 25 °C, [PMS] = 2 g L^{-1}, without pH adjustment.

10 M, the effect was nearly the same as that of 8 M. This may be attributed to that MeOH failed to capture the surface-bound radicals completely even at a high concentration. It was possible that
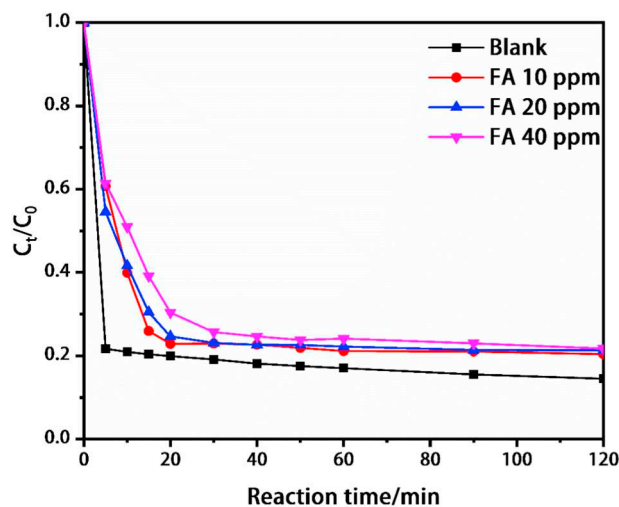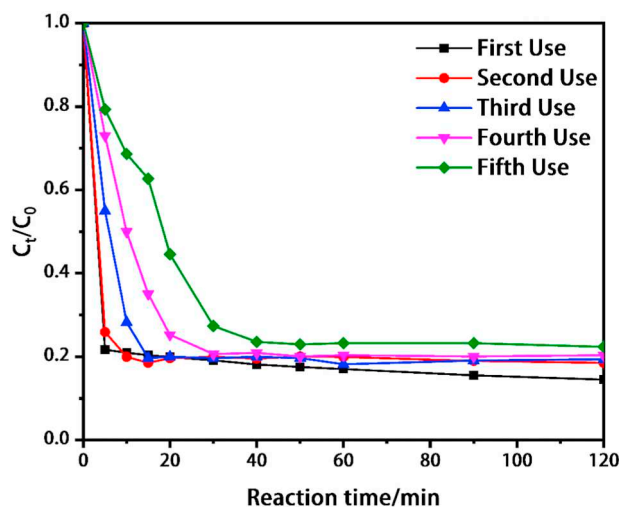
hydrophilic methanol was difficult to be extensively adsorbed on the surface of the nanomaterial, while the generated SO$_4$·$^-$ radicals could be surface-bounded (Wang et al., 2015a). Therefore, BQ was used instead of MeOH, because BQ can react with surface-bound free radicals (Yao et al., 2016). As shown in Fig. 9c, the addition of BQ inhibited the oxidation of LFX to some degree, indicating that surface-bound radicals played a positive impact in the degradation process.

The degradation experiments were also performed with methanol instead of aqueous solution. We can see from Fig. S5 that 18.5% of LFX was removed after 120 min in the MeOH experiment. It is deduced from the adsorption and MeOH experiments that non-radical oxidation pathway exists in the degradation of LFX. The N-doping can facilitate non-radical pathway, in which activated PMS molecules are capable of oxidizing LFX directly on the surface of the carbocatalysts without producing reactive radicals (Duan et al., 2016). This process has improved the effectiveness of LFX removal to some degree. However, compared with the previous experiments in aqueous solution, the degradation effect caused by non-radical oxidation was still far less than radical oxidation. Therefore, it can be concluded that SO$_4$·$^-$ and HO· are the dominant radicals during the catalytic process.

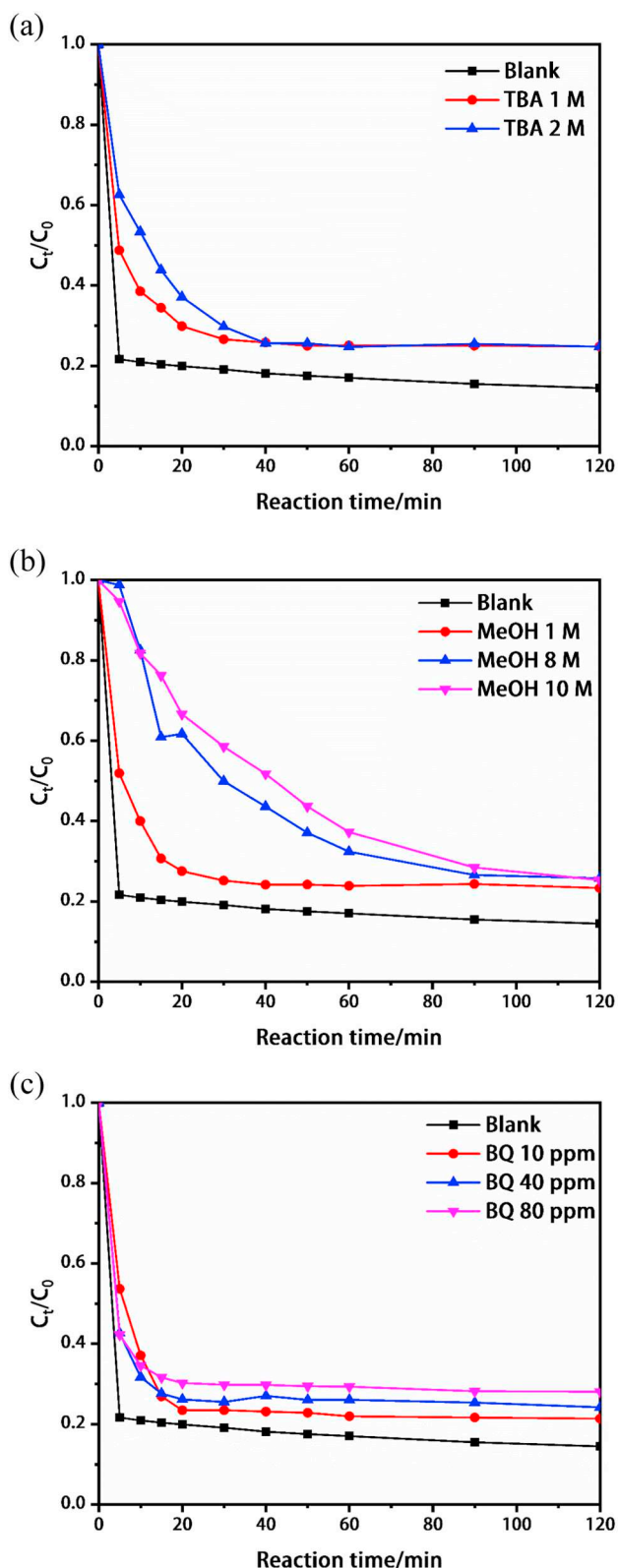We further observed a significant current decrease toward the B/N-

(a)

(b)

(c)

Fig. 9. Effects of different scavengers (a) TBA, (b) MeOH and (c) BQ on the degradation of LFX by the B/N-C@Fe$_{700}^4$/PMS process. The reaction conditions are: [LFX] = 50 mg L^{-1}, [catalyst] = 0.2 g L^{-1}, T = 25 °C, [PMS] = 2 g L^{-1}, without pH adjustment.

Fig. 10. Linear sweep voltammograms in the presence of PMS or/and LFX.

C@Fe4 700 electrode in the LSV analysis only when both PMS and LFX existed (Fig. 10). This observation reflected that interaction between PMS an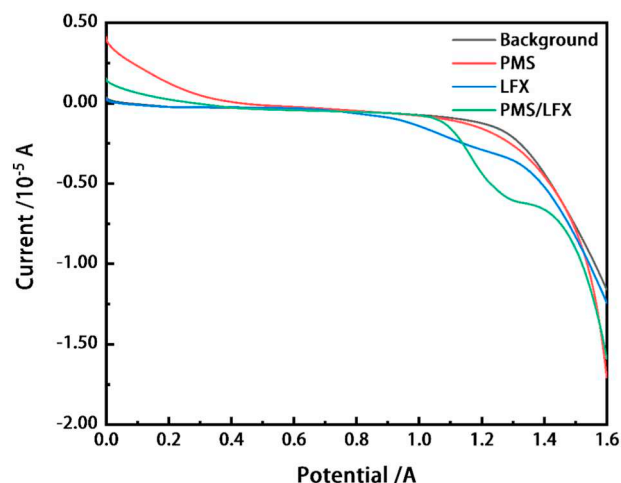d LFX on the surface of B/N-C@Fe4 700 is essential to facile electron transfer from LFX to PMS. Also, this result is consistent with the previous results about CNTs/PDS system based on the LSV result using a CNT electrode (Lee et al., 2015). After the injection of PMS, a slight decrease in current was detected due to the instant electron movement from the B/N-C@Fe4 700 electrode to PMS when PMS came into contact with the surface of B/N-C@Fe4 700, most likely through the formation of charge transfer (electron donor-acceptor) complex (Lee et al., 2016). Subsequently, upon the addition of LFX, a more remarkable decrease in current flow was observed, as electrons may transfer from LFX to the PMS/B/N-C@Fe4 700 complex similarly through the formation of charge transfer complex between B/N-C@Fe4 700 and PMS (Lee et al., 2016).

From the experimental results and the analyses above, the possible mechanisms for LFX degradation by the PMS/B/N-C@Fe4 700 system can be illustrated in Fig. 11. It is believed that both Fe^0 and Fe^{2+} can all activate PMS to generate large amounts of SO$_4$·$^-$. In comparison, Fe^0 exhibits a higher activity than Fe^{2+} and iron oxides, because Fe^0 can activate more SO$_4$·$^-$ than other forms of iron or iron oxides per mole (Sun et al., 2012). Furthermore, the Fe^{3+} involved in the as-synthesized nanomaterial B/N-C@Fe4 700 reacted with PMS to generate Fe^{2+}, thus promoting the production of SO$_4$·$^-$. In addition, HO· radicals can be activated in the presence of SO$_4$·$^-$ radicals among such aqueous system as well (Avetta et al., 2015).

4. Conclusions

In this study, the iron nanomaterials encapsulated within boron and nitrogen co-doped carbon nanoshell were synthesized through a simple and green pyrolysis process. The B/N-C@Fe/PMS system has a great application potential in the pharmaceutical wastewater treatment owing to its excellent catalytic performance and outstanding stability and reusability. The characterization results showed that Fe$_3$C nanocrystals were well encapsulated in the B/N co-doped carbon nanoshell and the transformation between Fe^{2+} and Fe^{3+} produced a large number of radicals for the LFX degradation. Quenching experiments suggested that SO$_4$·$^-$ and HO· were the major radicals (especially the former) for the catalytic degradation. The efficiency of the synthesized B/N-C@Fe in the fifth cycling still presented a comparable performance despite small amount of Fe leaching from the catalyst surface, which showed a promising potential in the practical application. Therefore, this study developed and proposed a novel way in preparing low-cost Fenton-like catalyst with porous carbon materials for advanced wastewater treatment.
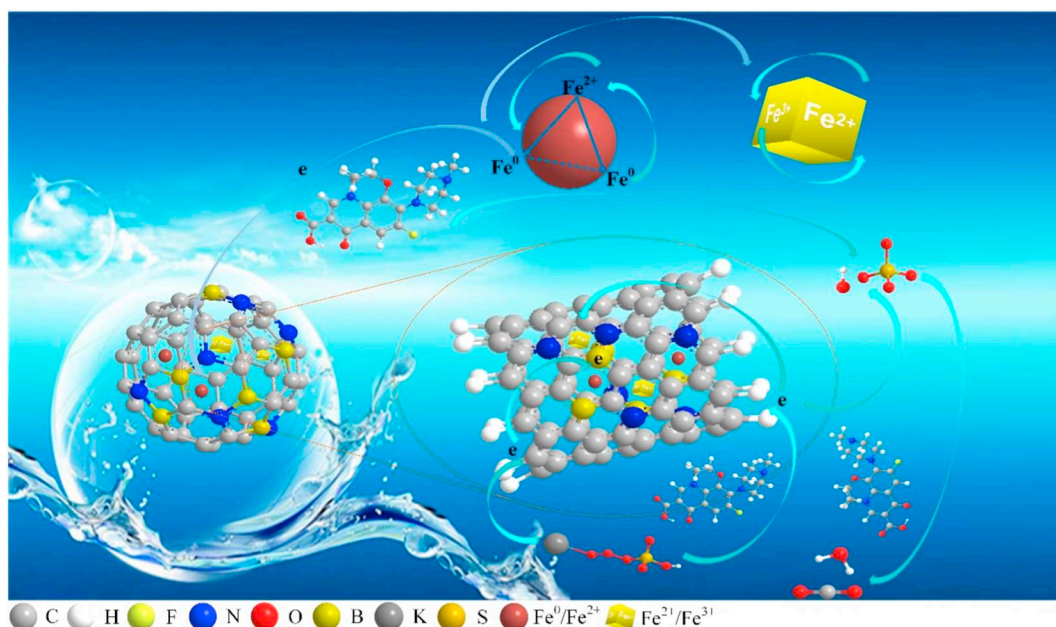
Fig. 11. Possible reaction mechanism for LFX degradation by the B/N-C@Fe/PMS system.

Acknowledgments

Appendix A. Supplementary data

Supplementary data to this article can be found online at https://doi.org/10.1016/j.envint.2019.04.006.

References

Ali, S., Liu, T.F., Lian, Z., Li, B., Su, D.S., 2017. The tunable effect of nitrogen and boron dopants on a single walled carbon nanotube support on the catalytic properties of a single gold atom catalyst: a first principles study of CO oxidation. J. Mater. Chem. A 5 (32), 16653–16662.

Anipsitakis, G.P., Dionysiou, D.D., 2003. Degradation of organic contaminants in water with sulfate radicals generated by the conjunction of peroxymonosulfate with cobalt. Environ. Sci. Technol. 37 (20), 4790–4797.

Avetta, P., Pensato, A., Minella, M., Malandrino, M., Maurino, V., Minero, C., Hanna, K., Vione, D., 2015. Activation of persulfate by irradiated magnetite: implications for the degradation of phenol under heterogeneous Photo-Fenton-Like conditions. Environ. Sci. Technol. 49 (2), 1043–1050.

Chen, S., Duan, J., Jaroniec, M., Qiao, S.-Z., 2014. Nitrogen and oxygen dual-doped carbon hydrogel film as a substrate-free electrode for highly efficient oxygen evolution reaction. Adv. Mater. 26 (18), 2925–2930.

Cui, X., Li, Y., Bachmann, S., Scalone, M., Surkus, A.-E., Junge, K., Topf, C., Beller, M., 2015. Synthesis and characterization of iron–nitrogen-doped graphene/core–shell catalysts: efficient oxidative dehydrogenation of N-Heterocycles. J. Am. Chem. Soc. 137 (33), 10652–10658.

Deng, J., Jiang, J., Zhang, Y., Lin, X., Du, C., Xiong, Y., 2008. FeVO4 as a highly active heterogeneous Fenton-like catalyst towards the degradation of Orange II. Appl. Catal. B Environ. 84 (3), 468–473.

Du, P., Eisenberg, R., 2012. Catalysts made of earth-abundant elements (Co, Ni, Fe) for water splitting: recent progress and future challenges. Energy Environ. Sci. 5 (3), 6012–6021.

Duan, X., Ao, Z., Sun, H., Indrawirawan, S., Wang, Y., Kang, J., Liang, F., Zhu, Z.H., Wang, S., 2015a. Nitrogen-doped graphene for generation and evolution of reactive radicals by metal-free catalysis. ACS Appl. Mater. Interfaces 7 (7), 4169–4178.

Duan, X., O'Donnell, K., Sun, H., Wang, Y., Wang, S., 2015b. Sulfur and nitrogen co-doped graphene for metal-free catalytic oxidation reactions. Small 11 (25), 3036–3044.

Duan, X., Ao, Z., Zhou, L., Sun, H., Wang, G., Wang, S., 2016. Occurrence of radical and nonradical pathways from carbocatalysts for aqueous and nonaqueous catalytic oxidation. Appl. Catal. B Environ. 188, 98–105.

Eskandarloo, H., Badiei, A., Behnajady, M.A., 2014. Study of the effect of additives on the photocatalytic degradation of a triphenylmethane dye in the presence of immobilized TiO2/NiO nanoparticles: artificial neural network modeling. Ind. Eng. Chem. Res. 53 (17), 6881–6895.

Ghosh Chaudhuri, R., Paria, S., 2012. Core/shell nanoparticles: classes, properties, synthesis mechanisms, characterization, and applications. Chem. Rev. 112 (4), 2373–2433.

Gong, K., Du, F., Xia, Z., Durstock, M., Dai, L., 2009. Nitrogen-doped carbon nanotube arrays with high electrocatalytic activity for oxygen reduction. Science 323 (5915), 760–764.

Goodwin, S.D., Gallis, H.A., Chow, A.T., Wong, F.A., Flor, S.C., Bartlett, J.A., 1994. Pharmacokinetics and safety of levofloxacin in patients with human-immunodeficiency-virus infection. Antimicrob. Agents Chemother. 38 (4), 799–804.

Guan, Y.-H., Ma, J., Ren, Y.-M., Liu, Y.-L., Xiao, J.-Y., Lin, L.-q., Zhang, C., 2013. Efficient degradation of atrazine by magnetic porous copper ferrite catalyzed peroxymonosulfate oxidation via the formation of hydroxyl and sulfate radicals. Water Res. 47 (14), 5431–5438.

Hamdi El Najjar, N., Touffet, A., Deborde, M., Journel, R., Leitner, N.K.V., 2013. Levofloxacin oxidation by ozone and hydroxyl radicals: kinetic study, transformation products and toxicity. Chemosphere 93 (4), 604–611.

Hu, Y., Jensen, J.O., Zhang, W., Cleemann, L.N., Xing, W., Bjerrum, N.J., Li, Q., 2014. Hollow spheres of iron carbide nanoparticles encased in graphitic layers as oxygen reduction catalysts. Angew. Chem. Int. Ed. 53 (14), 3675–3679.

Huang, W., Bianco, A., Brigante, M., Mailhot, G., 2018a. UVA-UVB activation of hydrogen peroxide and persulfate for advanced oxidation processes: efficiency, mechanism and effect of various water constituents. J. Hazard. Mater. 347, 279–287.

Huang, Z., Pan, H., Yang, W., Zhou, H., Gao, N., Fu, C., Li, S., Li, H., Kuang, Y., 2018b. In situ self-template synthesis of Fe–N-doped double-shelled hollow carbon microspheres for oxygen reduction reaction. ACS Nano 12 (1), 208–216.

Kang, J., Duan, X., Wang, C., Sun, H., Tan, X., Tade, M.O., Wang, S., 2018. Nitrogen-doped bamboo-like carbon nanotubes with Ni encapsulation for persulfate activation to remove emerging contaminants with excellent catalytic stability. Chem. Eng. J. 332, 398–408.

Khan, J.A., He, X., Khan, H.M., Shah, N.S., Dionysiou, D.D., 2013. Oxidative degradation of atrazine in aqueous solution by UV/H2O2/Fe2+, UV/S2O8 2−/Fe2+ and UV/HSO5 −/Fe2+ processes: A comparative study. Chem. Eng. J. 218, 376–383.

Kim, Y.A., Fujisawa, K., Muramatsu, H., Hayashi, T., Endo, M., Fujimori, T., Kaneko, K., Terrones, M., Behrends, J., Eckmann, A., Casiraghi, C., Novoselov, K.S., Saito, R., Dresselhaus, M.S., 2012. Raman spectroscopy of boron-doped single-layer graphene. ACS Nano 6 (7), 6293–6300.

Lee, H., Lee, H.-J., Jeong, J., Lee, J., Park, N.-B., Lee, C., 2015. Activation of persulfates by carbon nanotubes: oxidation of organic compounds by nonradical mechanism. Chem. Eng. J. 266, 28–33.

Lee, H., Kim, H.-i., Weon, S., Choi, W., Hwang, Y.S., Seo, J., Lee, C., Kim, J.-H., 2016. Activation of persulfates by graphitized nanodiamonds for removal of organic compounds. Environ. Sci. Technol. 50 (18), 10134–10142.

Lei, Y., Chen, C.-S., Tu, Y.-J., Huang, Y.-H., Zhang, H., 2015. Heterogeneous degradation

of organic pollutants by persulfate activated by $CuO-Fe_3O_4$: mechanism, stability, and effects of pH and bicarbonate ions. Environ. Sci. Technol. 49 (11), 6838–6845.

Lei, C., Sun, Y., Tsang, D.C.W., Lin, D., 2018. Environmental transformations and ecological effects of iron-based nanoparticles. Environ. Pollut. 232, 10–30.

Li, L.-X., Zhao, H.-W., Xing, T.-y., Geng, X., Song, R.-F., An, B.-G., 2018. Nitrogen-doped carbon coatings on carbon nanotubes as efficient oxygen reduction catalysts. Carbon 130, 843–844.

Liang, H.-W., Wei, W., Wu, Z.-S., Feng, X., Müllen, K., 2013. Mesoporous metal–nitrogen-doped carbon electrocatalysts for highly efficient oxygen reduction reaction. J. Am. Chem. Soc. 135 (43), 16002–16005.

Liu, X., Yang, D., Zhou, Y., Zhang, J., Luo, L., Meng, S., Chen, S., Tan, M., Li, Z., Tang, L., 2017. Electrocatalytic properties of N-doped graphite felt in electro-Fenton process and degradation mechanism of levofloxacin. Chemosphere 182, 306–315.

Miklos, D.B., Remy, C., Jekel, M., Linden, K.G., Drewes, J.E., Hübner, U., 2018. Evaluation of advanced oxidation processes for water and wastewater treatment – a critical review. Water Res. 139, 118–131.

Peng, H., Liu, F., Liu, X., Liao, S., You, C., Tian, X., Nan, H., Luo, F., Song, H., Fu, Z., Huang, P., 2014. Effect of transition metals on the structure and performance of the doped carbon catalysts derived from polyaniline and melamine for ORR application. ACS Catal. 4 (10), 3797–3805.

Ratso, S., Käärik, M., Kook, M., Paiste, P., Kisand, V., Vlassov, S., Leis, J., Tammeveski, K., 2018. Iron and nitrogen co-doped carbide-derived carbon and carbon nanotube composite catalysts for oxygen reduction reaction. ChemElectroChem 5 (14), 1827–1836.

Sharma, R., Kumar, V., Bansal, S., Singhal, S., 2015. Assortment of magnetic nanospinels for activation of distinct inorganic oxidants in photo-Fenton's process. J. Mol. Catal. A Chem. 402, 53–63.

Shen, M., Ruan, C., Chen, Y., Jiang, C., Ai, K., Lu, L., 2015. Covalent entrapment of cobalt–iron sulfides in N-doped mesoporous carbon: extraordinary bifunctional electrocatalysts for oxygen reduction and evolution reactions. ACS Appl. Mater. Interfaces 7 (2), 1207–1218.

Shi, J., Wang, Y., Du, W., Hou, Z., 2016. Synthesis of graphene encapsulated Fe_3C in carbon nanotubes from biomass and its catalysis application. Carbon 99, 330–337.

Soares, O.S.G.P., Rocha, R.P., Gonçalves, A.G., Figueiredo, J.L., Órfão, J.J.M., Pereira, M.F.R., 2015. Easy method to prepare N-doped carbon nanotubes by ball milling. Carbon 91, 114–121.

Su, C., Puls, R.W., 2004. Nitrate reduction by zerovalent iron: effects of formate, oxalate, citrate, chloride, sulfate, borate, and phosphate. Environ. Sci. Technol. 38 (9), 2715–2720.

Sun, H., Zhou, G., Liu, S., Ang, H.M., Tadé, M.O., Wang, S., 2012. Nano-Fe^0 encapsulated in microcarbon spheres: synthesis, characterization, and environmental applications. ACS Appl. Mater. Interfaces 4 (11), 6235–6241.

Sun, H., Kwan, C., Suvorova, A., Ang, H.M., Tadé, M.O., Wang, S., 2014. Catalytic oxidation of organic pollutants on pristine and surface nitrogen-modified carbon nanotubes with sulfate radicals. Appl. Catal. B Environ. 154–155, 134–141.

Sun, Y., Lei, C., Khan, E., Chen, S.S., Tsang, D.C.W., Ok, Y.S., Lin, D., Feng, Y., Li, X.D., 2017. Nanoscale zero-valent iron for metal/metalloid sequestration from hydraulic fracturing wastewater. Chemosphere 176, 315–323.

Sun, Y., Lei, C., Khan, E., Chen, S.S., Tsang, D.C.W., Ok, Y.S., Lin, D., Feng, Y., Li, X.D., 2018. Aging effects on chemical transformation and metal(loid) removal by entrapped nanoscale zero-valent iron for hydraulic fracturing wastewater treatment. Sci. Total Environ. 615, 498–507.

Sun, Y., Yu, I.K.M., Tsang, D.C.W., Cao, X., Lin, D., Wang, L., Graham, N.J.D., Alessi, D.S., Komarek, M., Ok, Y.S., Feng, Y., Li, X.D., 2019. Multifunctional iron-biochar composites for the removal of potentially toxic elements, inherent cations, and heterochloride from hydraulic fracturing wastewater. Environ. Int. 124, 521–532.

Tran, N.H., Reinhard, M., Gin, K.Y.-H., 2018. Occurrence and fate of emerging contaminants in municipal wastewater treatment plants from different geographical regions-a review. Water Res. 133, 182–207.

Tso, C.-P., Shih, Y.-H., 2015. The reactivity of well-dispersed zerovalent iron nanoparticles toward pentachlorophenol in water. Water Res. 72, 372–380.

Tso, C.-P., Shih, Y.-H., 2018. Effect of carboxylic acids on the properties of zerovalent iron toward adsorption and degradation of trichloroethylene. J. Environ. Manag. 206, 817–825.

Van Doorslaer, X., Dewulf, J., Van Langenhove, H., Demeestere, K., 2014. Fluoroquinolone antibiotics: An emerging class of environmental micropollutants. Sci. Total Environ. 500-501, 250–269.

Wang, J., Zheng, S., Shao, Y., Liu, J., Xu, Z., Zhu, D., 2010a. Amino-functionalized $Fe_3O_4@SiO_2$ core–shell magnetic nanomaterial as a novel adsorbent for aqueous heavy metals removal. J. Colloid Interface Sci. 349 (1), 293–299.

Wang, L., Ying, G.-G., Zhao, J.-L., Yang, X.-B., Chen, F., Tao, R., Liu, S., Zhou, L.-J., 2010b. Occurrence and risk assessment of acidic pharmaceuticals in the Yellow River, Hai River and Liao River of north China. Sci. Total Environ. 408 (16), 3139–3147.

Wang, C., Guo, Z., Shen, W., Xu, Q., Liu, H., Wang, Y., 2014a. B-doped carbon coating improves the electrochemical performance of electrode materials for Li-ion batteries. Adv. Funct. Mater. 24 (35), 5511–5521.

Wang, Y., Sun, H., Ang, H.M., Tadé, M.O., Wang, S., 2014b. Magnetic Fe_3O_4/carbon sphere/cobalt composites for catalytic oxidation of phenol solutions with sulfate radicals. Chem. Eng. J. 245, 1–9.

Wang, X., Qin, Y., Zhu, L., Tang, H., 2015a. Nitrogen-doped reduced graphene oxide as a bifunctional material for removing bisphenols: synergistic effect between adsorption and catalysis. Environ. Sci. Technol. 49 (11), 6855–6864.

Wang, Y., Sun, H., Duan, X., Ang, H.M., Tadé, M.O., Wang, S., 2015b. A new magnetic

nano zero-valent iron encapsulated in carbon spheres for oxidative degradation of phenol. Appl. Catal. B Environ. 172-173, 73–81.

Wang, C., Kang, J., Sun, H., Ang, H.M., Tadé, M.O., Wang, S., 2016a. One-pot synthesis of N-doped graphene for metal-free advanced oxidation processes. Carbon 102, 279–287.

Wang, C., Shi, P., Cai, X., Xu, Q., Zhou, X., Zhou, X., Yang, D., Fan, J., Min, Y., Ge, H., Yao, W., 2016b. Synergistic effect of Co_3O_4 nanoparticles and graphene as catalysts for peroxymonosulfate-based orange II degradation with high oxidant utilization efficiency. J. Phys. Chem. C 120 (1), 336–344.

Wang, C., Kang, J., Liang, P., Zhang, H., Sun, H., Tade, M.O., Wang, S., 2017. Ferric carbide nanocrystals encapsulated in nitrogen-doped carbon nanotubes as an outstanding environmental catalyst. Environ. Sci.: Nano 4 (1), 170–179.

Wang, Q., Ge, X., Xu, J., Du, Y., Zhao, X., Si, L., Zhou, X., 2018. Fabrication of microporous sulfur-doped carbon microtubes for high-performance sodium-ion batteries. ACS Appl. Energy Materi. 1 (11), 6638–6645.

Wang, L., Cho, D.-W., Tsang, D.C.W., Cao, X., Hou, D., Shen, Z., Alessi, D.S., Ok, Y.S., Poon, C.S., 2019. Green remediation of As and Pb contaminated soil using cement-free clay-based stabilization/solidification. Environ. Int. 126, 336–345.

Wei, G., Liang, X., He, Z., Liao, Y., Xie, Z., Liu, P., Ji, S., He, H., Li, D., Zhang, J., 2015. Heterogeneous activation of oxone by substituted magnetites $Fe_{3−x}O_4$ (Cr, Mn, Co, Ni) for degradation of acid orange II at neutral pH. J. Mol. Catal. A Chem. 398, 86–94.

Wu, Z.-S., Yang, S., Sun, Y., Parvez, K., Feng, X., Müllen, K., 2012. 3D nitrogen-doped graphene aerogel-supported Fe_3O_4 nanoparticles as efficient electrocatalysts for the oxygen reduction reaction. J. Am. Chem. Soc. 134 (22), 9082–9085.

Xiao, M., Zhu, J., Feng, L., Liu, C., Xing, W., 2015. Meso/macroporous nitrogen-doped carbon architectures with iron carbide encapsulated in graphitic layers as an efficient and robust catalyst for the oxygen reduction reaction in both acidic and alkaline solutions. Adv. Mater. 27 (15), 2521–2527.

Xiong, X., Yu, I.K.M., Cao, L., Tsang, D.C.W., Zhang, S., Ok, Y.S., 2017. A review of biochar-based catalysts for chemical synthesis, biofuel production, and pollution control. Bioresour. Technol. 246, 254–270.

Xu, K., Ben, W., Ling, W., Zhang, Y., Qu, J., Qiang, Z., 2017. Impact of humic acid on the degradation of levofloxacin by aqueous permanganate: kinetics and mechanism. Water Res. 123, 67–74.

Yan, S.C., Li, Z.S., Zou, Z.G., 2010. Photodegradation of Rhodamine B and methyl Orange over boron-doped g-C_3N_4 under visible light irradiation. Langmuir 26 (6), 3894–3901.

Yan, B., Niu, C.H., Wang, J., 2017. Analyses of levofloxacin adsorption on pretreated barley straw with respect to temperature: kinetics, π–π electron-donor–acceptor interaction and site energy distribution. Environ. Sci. Technol. 51 (14), 8048–8056.

Yao, Y., Cai, Y., Wu, G., Wei, F., Li, X., Chen, H., Wang, S., 2015a. Sulfate radicals induced from peroxymonosulfate by cobalt manganese oxides ($Co_xMn_{3−x}O_4$) for Fenton-Like reaction in water. J. Hazard. Mater. 296, 128–137.

Yao, Y., Lu, F., Zhu, Y., Wei, F., Liu, X., Lian, C., Wang, S., 2015b. Magnetic core–shell $CuFe_2O_4@C_3N_4$ hybrids for visible light photocatalysis of Orange II. J. Hazard. Mater. 297, 224–233.

Yao, Y.J., Chen, H., Qin, J.C., Wu, G.D., Lian, C., Zhang, J., Wang, S.B., 2016. Iron encapsulated in boron and nitrogen codoped carbon nanotubes as synergistic catalysts for Fenton-like reaction. Water Res. 101, 281–291.

Yu, I.K.M., Xiong, X., Tsang, D.C.W., Wang, L., Hunt, A.J., Song, H., Shang, J., Ok, Y.S., Poon, C.S., 2019. Aluminium-biochar composite as a sustainable heterogeneous catalyst for glucose isomerization in biorefinery. Green Chem. 21, 1267–1281.

Zeng, T., Zhang, X., Wang, S., Niu, H., Cai, Y., 2015. Spatial confinement of a Co_3O_4 catalyst in hollow metal–organic frameworks as a nanoreactor for improved degradation of organic pollutants. Environ. Sci. Technol. 49 (4), 2350–2357.

Zhang, T., Zhu, H., Croué, J.-P., 2013. Production of sulfate radical from peroxymonosulfate induced by a magnetically separable $CuFe_2O_4$ spinel in water: efficiency, stability, and mechanism. Environ. Sci. Technol. 47 (6), 2784–2791.

Zhang, J., Byeon, A., Lee, J.W., 2014. Boron-doped carbon-iron nanocomposites as efficient oxygen reduction electrocatalysts derived from carbon dioxide. Chem. Commun. 50 (48), 6349–6352.

Zhang, J., Nie, N., Liu, Y., Wang, J., Yu, F., Gu, J., Li, W., 2015a. Boron and nitrogen codoped carbon layers of $LiFePO_4$ improve the high-rate electrochemical performance for lithium ion batteries. ACS Appl. Mater. Interfaces 7 (36), 20134–20143.

Zhang, Q.-Q., Ying, G.-G., Pan, C.-G., Liu, Y.-S., Zhao, J.-L., 2015b. Comprehensive evaluation of antibiotics emission and fate in the river basins of China: source analysis, multimedia modeling, and linkage to bacterial resistance. Environ. Sci. Technol. 49 (11), 6772–6782.

Zhang, W., Zhou, S., Sun, J., Meng, X., Luo, J., Zhou, D., Crittenden, J., 2018. Impact of chloride ions on UV/H_2O_2 and UV/persulfate advanced oxidation processes. Environ. Sci. Technol. 52 (13), 7380–7389.

Zhao, Q., Mao, Q., Zhou, Y., Wei, J., Liu, X., Yang, J., Luo, L., Zhang, J., Chen, H., Chen, H., Tang, L., 2017. Metal-free carbon materials-catalyzed sulfate radical-based advanced oxidation processes: a review on heterogeneous catalysts and applications. Chemosphere 189, 224–238.

Zhou, L., Shao, Y., Liu, J., Ye, Z., Zhang, H., Ma, J., Jia, Y., Gao, W., Li, Y., 2014. Preparation and characterization of magnetic porous carbon microspheres for removal of methylene blue by a heterogeneous Fenton reaction. ACS Appl. Mater. Interfaces 6 (10), 7275–7285.

Zhou, Y., Jiang, J., Gao, Y., Ma, J., Pang, S.-Y., Li, J., Lu, X.-T., Yuan, L.-P., 2015. Activation of peroxymonosulfate by benzoquinone: a novel nonradical oxidation process. Environ. Sci. Technol. 49 (21), 12941–12950.

Zhou, Y., Liu, X., Xiang, Y., Wang, P., Zhang, J., Zhang, F., Wei, J., Luo, L., Lei, M., Tang, L., 2017. Modification of biochar derived from sawdust and its application in removal of tetracycline and copper from aqueous solution: adsorption mechanism and modelling. Bioresour. Technol. 245, 266–273.

Zhou, Y., Wu, S., Zhou, H., Huang, H., Zhao, J., Deng, Y., Wang, H., Yang, Y., Yang, J., Luo, L., 2018a. Chiral pharmaceuticals: environment sources, potential human health impacts, remediation technologies and future perspective. Environ. Int. 121, 523–537.

Zhou, Y., Xiang, Y., He, Y., Yang, Y., Zhang, J., Luo, L., Peng, H., Dai, C., Zhu, F., Tang, L., 2018b. Applications and factors influencing of the persulfate-based advanced oxidation processes for the remediation of groundwater and soil contaminated with organic compounds. J. Hazard. Mater. 359, 396–407.

Zou, J., Ma, J., Chen, L., Li, X., Guan, Y., Xie, P., Pan, C., 2013. Rapid acceleration of ferrous iron/peroxymonosulfate oxidation of organic pollutants by promoting Fe(III)/Fe(II) cycle with hydroxylamine. Environ. Sci. Technol. 47 (20), 11685–11691.